

# CREEP STRENGTH AND MICROSTRUCTURE OF POLYCRYSTALLINE $\gamma'$ -STRENGTHENED COBALT-BASE SUPERALLOYS

Alexander Bauer<sup>1</sup>, Steffen Neumeier<sup>1</sup>, Florian Pyczak<sup>2</sup>, Mathias Göken<sup>1</sup>

<sup>1</sup>Department of Materials Science & Engineering, Institute I: General Materials Properties,  
University Erlangen-Nürnberg, Erlangen, 91058, Germany

<sup>2</sup>Helmholtz-Zentrum Geesthacht, Centre for Materials and Coastal Research, Geesthacht, 21502, Germany

Keywords: superalloy, cobalt, creep, boron, grain boundary strengthening

## Abstract

The influence of several alloying elements on the microstructure and creep properties of polycrystalline Co-base superalloys hardened with the ternary  $L1_2$  compound,  $\gamma'$ -Co<sub>3</sub>(Al,W), are presented in this work. The stability of the  $\gamma/\gamma'$ -microstructure was investigated by long term aging at temperatures of 750 °C and 900 °C. High contents of chromium and iron destabilize the  $\gamma/\gamma'$ -microstructure. Additions of nickel widen the  $\gamma/\gamma'$ - two phase field. Discontinuous precipitation is observed only in the iridium-containing alloy during aging. In all other alloys no formation of further intermetallic phases are found even after 1000 hrs aging at 750 °C and 900 °C. Boron has been added for the formation of grain boundary strengthening intermetallic phases which leads to an adjacent  $\gamma'$ -depleted zone. Nanoindentation shows that titanium improves its hardness. The creep strength of the studied alloys is sufficiently better than that of commercial carbide hardened polycrystalline Co-base superalloys and already close to  $\gamma'$ -hardened Ni-base superalloys. An alloy containing 2 at.% titanium exhibited a creep strength comparable with the Ni-base alloy IN100. The microstructure after creep tests at 950 °C showed rafting perpendicular to the compressive load axis, confirming the positive lattice misfit of the alloys at high temperatures which was determined with high energy X-ray diffraction.

## Introduction

Engineering materials for use in the combustion zone of turbine engines have to withstand not only high mechanical loads at elevated temperatures, but also a severe oxidative environment. Materials for vanes, blades and discs which fulfill these demands are nowadays Ni-base superalloys. Due to their unique two-phase  $\gamma/\gamma'$ -microstructure consisting of a  $L1_2$  ordered intermetallic compound ( $\gamma'$ -phase/Ni<sub>3</sub>Al) coherently embedded into a Al matrix ( $\gamma$ -phase/Ni solid solution) they exhibit excellent high temperature strength [1]. The recent discovery of the new ternary  $L1_2$  intermetallic compound Co<sub>3</sub>(Al,W) by Sato et al. [2] opened new possibilities in the development of Co-base superalloys. Before then, only a thermally unstable  $\gamma'$ -phase or a  $\gamma'$ -phase with very high misfit have been known, which are unsuitable for high temperature strengthening [1, 3]. In the following years after the discovery by Sato this alloy class has been intensively investigated in terms of phase stability [4, 5, 6], mechanical properties [7, 8, 9], oxidation resistance [10, 11] as well as atomic structure [12, 13]. First creep tests revealed that already a very simple Co-Al-W-alloy with Ti showed a creep strength comparable to that of Ni-base alloys [9, 14]. First XRD measurements by Sato et al. have shown that the lattice misfit at room temperatures is positive [2]. However, from Ni-base superalloys it is known that the lattice misfit changes significantly

with increasing temperature [15, 16]. Therefore, it has to be investigated whether the lattice parameter of the  $\gamma'$ -phase stays larger than that one of  $\gamma$ -phase with increasing temperature or becomes zero or even negative. A positive misfit at application temperature would lead to a rafted  $\gamma/\gamma'$ -microstructure oriented parallel to the applied tensile stress axis, which could be beneficial in terms of fatigue properties.

Ta and Ti were shown to substantially increase the volume fraction of the  $\gamma'$ -phase as well as its solvus temperature. Both elements also greatly enhance the mechanical properties [7, 14].

The addition of boron was found to be beneficial in terms of tensile and creep properties [8, 9, 14] due to formation of tungsten borides increasing the grain boundary strength. An adjacent particle depleted zone forms due to depletion of tungsten, which is crucial for the formation of the Co<sub>3</sub>(Al,W) compound [14].

This work contributes to the further development of this material system by microstructural investigations and creep tests on several boron-containing alloys with additional alloying elements.

The microstructure of long term aged samples was investigated in terms of phase stability of the phases present. The  $\gamma'$ -depleted area along the grain boundary precipitates was investigated using nanoindentation in order to correlate results on creep strength and grain boundary strength. Nanoindentation was shown in literature as a suitable method to investigate mechanical properties on a local scale [17]. Synchrotron diffraction experiments were performed to determine the lattice misfit at creep temperature. The results were correlated with the microstructure after creep deformation and its rafting behavior.

## Experimental

All polycrystalline alloys were arc melted from technically pure metals or corresponding master alloys. The nominal compositions are given in Table 1. Glow discharge optical emission spectroscopy (GDOES) was utilized to confirm the boron content, because it is not reliable measurable with energy dispersive X-ray spectroscopy (EDS). Also the amount of Si was determined from GDOES measurements as the overlapping element lines of Si and W make the EDS measurement of Si-content difficult in this system. GDOES measurements were performed on a RF GD Profiler (HORIBA Jobin Yvon) equipped with a 4-mm-diameter anode operating at a radio frequency of 13.56 MHz and a power of 50 W. High-purity argon (99.9999 %) was used as a discharge gas at a pressure of 700 Pa.

All alloys were solution heat treated at 1300 °C for 12 hrs and aged at 900 °C for 200 hrs. Additional investigations of the long term stability were conducted on solution heat treated samples encapsulated in argon atmosphere and aged at 750 °C and 900 °C for 1000 hrs, respectively.

Table 1: Investigated Co-base superalloys. EDS data were determined on solution heat treated samples. See also [9, 14]. Compositions marked with “\*” could not be determined using EDS. However, GDOES measurements confirmed the nominal Si content. Additional alloying elements are given in column “X”. The volume fraction of the  $\gamma'$ -phase was determined by stereological methods.

Utilized abbreviations	Nominal composition	Measured composition / at. %						Transformation temperatures / °C			$\gamma'$ vol. fr. /%
		Co	Al	W	Cr	Ta	X	Solvus	Solidus	Liquidus	
9W-0.04B	Co-9Al-9W-0.04B	81.9	8.4	9.7	-	-	-	986	1440	1467	58
9W-0.08B	Co-9Al-9W-0.08B	81.5	8.9	9.5	-	-	-	984	1439	1465	58
9W-0.12B	Co-9Al-9W-0.12B	82.2	8.3	9.4	-	-	-	982	1444	1469	58
9W-2Ta-0.12B	Co-9Al-9W-2Ta-0.12B	79.8	8.9	9.3	-	2.0	-	1097	1410	1434	82
9W-1Mo-0.04B	Co-9Al-9W-1Mo-0.04B	81.2	8.2	9.4	-	-	1.1	994	1436	1461	72
10W-2Si	Co-9Al-10W-2Si	81.0	8.7	10.3	-	-	0*	998	1415	1449	72
9W-2Ti-0.12B	Co-9Al-9W-2Ti-0.12B	79.8	8.4	9.6	-	-	2.2	1080	1414	1434	75
9W-2Cr-0.04B [14]	Co-9Al-9W-2Cr-0.04B	80.5	8.1	9.4	2.0	-	-	975	1439	1464	65
9W-4Cr-0.04B [11]	Co-9Al-9W-4Cr-0.04B	77.8	8.6	9.5	4.1	-	-	977	1425	1454	83
9W-8Cr-0.04B [11]	Co-9Al-9W-8Cr-0.04B	73.8	8.7	9.3	8.2	-	-	947	1412	1440	-
9W-16Cr-0.04B	Co-9Al-9W-16Cr-0.04B	66.0	8.4	9.0	16.5	-	-	860	1372	1409	-
9W-9Ni-0.12B	Co-9Al-9W-9Ni-0.12B	72.8	8.8	9.5	-	-	9.0	--	--	--	59
9W-18Ni-0.12B	Co-9Al-9W-18Ni-0.12B	63.3	8.8	9.6	-	-	18.4	--	--	--	76
9W-8Cr-9Ni-0.12B	Co-9Al-9W8Cr-9Ni-0.12B	64.3	9.1	9.3	8.2	-	9.2	958	1418	1439	61
9W-8Cr-18Ni-0.12B	Co-9Al-9W-8Cr-18Ni-0.12B	56.5	8.6	8.8	8.1	-	18.0	978	1420	1441	45
8W-2Ta-2Ir [9]	Co-9Al-8W-2Ta-2Ir	78.6	8.1	9.1	-	1.7	2.5	1137	1426	1454	80
5W-2Ta-2Ir [9]	Co-9Al-5.5W-2Ta-2Ir	83.5	8.7	5.5	-	1.3	0.9	1060	1418	1452	54
9W-8Fe-0.12B	Co-9Al-9W-8Fe-0.12B	75.7	7.5	8.8	-	-	8.0	932	1431	1453	-
9W-16Fe-0.12B	Co-9Al-9W-16Fe-0.12B	66.2	8.6	8.6	-	-	16.7	877	1427	1450	-

Measurements of the transformation temperatures were performed on a Netzsch STA 409 CD. Samples with a mass of about 300 mg were investigated with a heating/cooling rate of 5 Kmin<sup>-1</sup>.

Microstructure characterization was done on a Zeiss Crossbeam 1540 EsB focused ion beam instrument with an Oxford Instruments EDS system. Mechanically polished samples were etched with a Vogel's Spar solution (100 ml of distilled water, 100 ml of 32 % HCl, 10 ml of 65 % HNO<sub>3</sub> and 0.3 ml of Dr. Vogel's Spar etchant consisting of 30-50% 1-methoxy-2-propanol and 2.5 % - 5 % thiocarbamide).

Creep experiments in compression mode were performed in air at temperatures between 850 °C and 950 °C on cylindrical specimens with a geometry of 7.5 mm in height and 5 mm in diameter at a constant stress range (80 MPa to 500 MPa). Tests were conducted to a maximum plastic strain of about 5 %.

Nanoindentation hardness measurements were performed using a Triboscope nanoindenter from Hysitron installed into a multimode AFM from Veeco for evaluation of local mechanical properties. Indentations were carried out up to a maximum load of 250  $\mu$ N. Hardness was determined by analyzing the load-displacement curves according to Oliver-Pharr method [18], [19]. For determining the lattice misfit of the ternary alloy 9W-0.12B at

room temperature and at 850 °C high energy X-ray diffraction experiments at the High Energy Materials Science (HEMS) beamline of the Helmholtz-Zentrum Geesthacht at the PETRA III storage ring of DESY in Hamburg, Germany, were performed. A specimen with a diameter of 5 mm was investigated in transmission geometry with a photon energy of 87 keV ( $\lambda = 0.1425$  Å). The resulting reflections were recorded on a Mar345 image plate detector. For high temperature measurements the sample was heated in an induction furnace under argon atmosphere during the measurement. The (002) reflections were recorded, which are a combination of the sub-peaks of the  $\gamma$ - and  $\gamma'$ -phase. By fitting the respective sub-peaks to the overall shape of the (002) peak using Pseudo Voigt functions the lattice constants of the  $\gamma$  and  $\gamma'$  phases could be determined. From the lattice constants of the phases  $\gamma$  and  $\gamma'$ ,  $a_\gamma$  and  $a_{\gamma'}$ , the lattice misfit  $\delta$  was calculated by the following formula:

$$\delta = \frac{2(a_{\gamma'} - a_\gamma)}{a_{\gamma'} + a_\gamma} \quad (1)$$

Table 2: Reference alloys. Compositions are given in atomic percent.

Alloy	Ni	Co	Cr	Mo	W	Al	Ti	Ta	Fe	Mn	C	B	Zr
IN100 [20]	56.8	13.8	10.4	1.7	-	11.0	5.3	-	-	-	0.8	0.07	0.04
Mar-M 509 [21]	10.2	57.9	24.9	-	2.3	-	0.3	1.2	-	-	3	-	0.3

## Results and Discussion

### Microstructure – alloying elements

The simple ternary alloy Co-9Al-9W with boron additions shows the well-known two-phase microstructure (Figure 1) as reported

by Sato et al. analogous to  $\gamma'$ -strengthened Ni-base superalloys with very similar morphology and  $\gamma'$  volume fraction [2]. Even though the  $\gamma/\gamma'$  two-phase field in the Co-Al-W phase diagram [2] is relatively small, minor additions of other alloying elements to the ternary composition are feasible and can improve the high temperature properties like yield and creep strength as well as the

oxidation resistance [7, 9, 10]. In general, the partitioning behavior of the alloying elements is similar to Ni-base superalloys [22]. The effects of different alloying elements in  $\gamma'$ -hardened Co-base alloys will be discussed below in more detail.

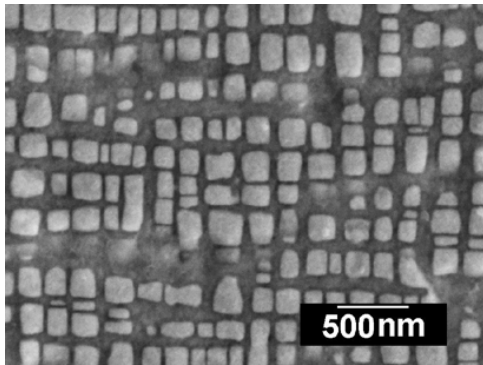


Figure 1:  $\gamma/\gamma'$ -microstructure of the ternary Co-base superalloy 9W-0.04B.

**Chromium** is a crucial element in Ni-base superalloys and in conventional carbide hardened Co-base alloys since Cr leads to excellent oxidation and corrosion resistance [1]. However, an increasing Cr content has an unfavorable influence on the  $\gamma/\gamma'$ -microstructure in the new  $\gamma'$ -strengthened Co-base alloy class. With increasing contents of Cr up to 4 at.% the  $\gamma'$ -volume fraction increases and the precipitates become more cubic compared to the ternary alloy (compare Figure 1 with Figure 2a and 2b).

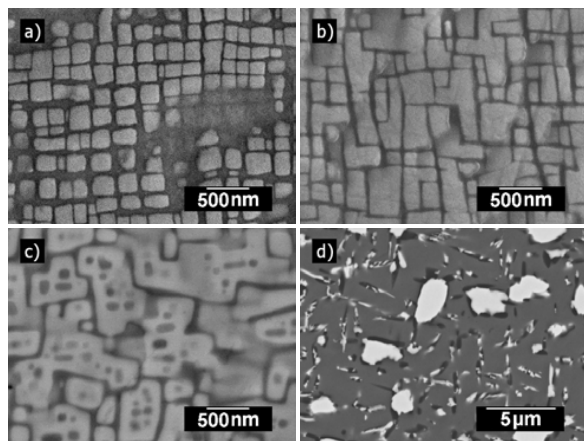


Figure 2: Microstructure of Cr containing alloys. a) 9W-2Cr-0.04B, b) 9W-4Cr-0.04B, c) 9W-8Cr-0.04B, d) 9W-16Cr-0.04B

However, with 8 at.% Cr the shape of the  $\gamma'$ -precipitates becomes more rounded again (see Figure 2c). In literature, it is reported that Cr partitions preferably to the  $\gamma$ -phase [2, 23]. Assuming that Cr has a similar Vegard's coefficient in Co compared to Ni [20] it should increase the lattice parameter of  $\gamma$  more than that of  $\gamma'$ . Therefore Cr should lead to a decreasing  $\gamma'$ -volume fraction and  $\gamma/\gamma'$ -lattice misfit. Accordingly, the increased  $\gamma'$ -volume fraction and more cubic precipitate shape up to 4 at.% can only be explained by a changed partitioning behavior of W which is shifted towards the  $\gamma'$ -phase and essential for its formation. With a Cr content of 8 at.% further W-rich intermetallic phases appear (Figure 3) which decrease the content of W and might be the reason for the changed trend.

Finally, addition of 16 at.% of Cr leads to a complete transformation of the  $\gamma/\gamma'$ -microstructure to a three phase microstructure as shown in Figure 2d. Since Cr also decreases the  $\gamma'$ -solvus temperature (Table 1), its content in the alloys has to be balanced with elements capable of increasing the  $\gamma'$ -solvus temperature.

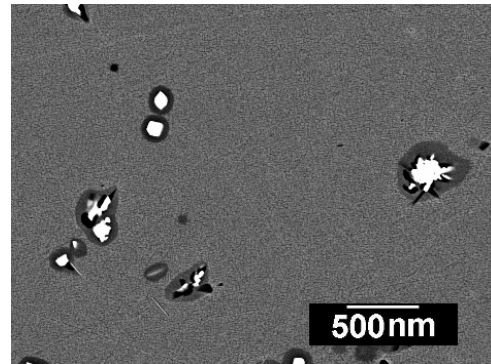


Figure 3: Tungsten rich precipitates in the 9W-8Cr-0.12B alloy after aging for 200hrs.

A possible way to enlarge the  $\gamma/\gamma'$  two-phase field is alloying of **nickel** as reported by Shinagawa et al. [4]. In the present work, two alloys with Ni additions of 9 at.% and 18 at.% have been investigated. As seen in Figure 4, the volume fraction of the  $\gamma'$ -phase increased and no other intermetallic phases besides the  $\gamma$  and  $\gamma'$  phases were observed even in the Ni-rich alloy. Additionally, with increasing Ni content there is a noticeable increase in the  $\gamma'$ -solvus temperature [4]. According to Shinagawa et al. the lattice misfit after addition of 9 at.% and 18 at.% is supposed to decrease only slightly from about 0.42 % to approximately 0.38 %, respectively. Therefore, no significant change in the  $\gamma'$ -precipitate shape is expected which is consistent with the microstructural observations shown in Figure 4.

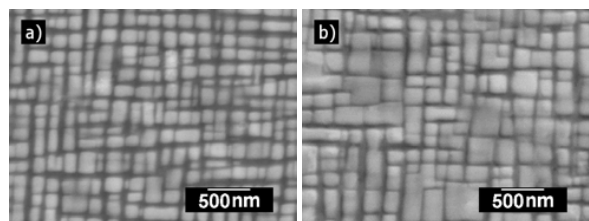


Figure 4: Microstructure of Ni containing alloys. a) 9W-9Ni-0.12B, b) 9W-18Ni-0.12B

Addition of 8 at.% of Cr to both of the Ni-containing alloys (Figure 5) proved the widening of the  $\gamma/\gamma'$  two-phase field by Ni since no further intermetallic phases were observed in contrast to the Ni free 9W-8Cr-0.04B alloy.

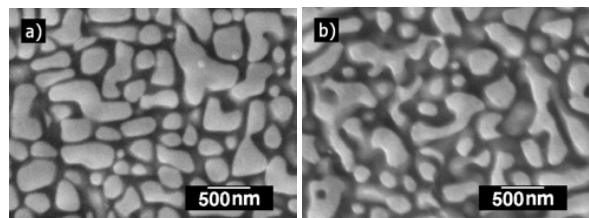


Figure 5: Microstructure of alloys containing Ni and Cr. a) 9W-8Cr-9Ni-0.12B, b) 9W-8Cr-18Ni-0.12B.

However, the  $\gamma'$ -volume fraction decreased with increasing Ni content possibly due to the change in partitioning behavior of W as found by Shinagawa et al. [4]. The rounded shape of the  $\gamma'$ -precipitates is a hint to a change in the lattice misfit. This is also consistent with [4] stating that the lattice misfit decreases with increasing Ni content. In order to obtain a well-ordered  $\gamma/\gamma'$ -microstructure with cuboidal  $\gamma'$ -precipitates further adjustment of the chemical composition of  $\gamma'$ -strengthened Co-base superalloys containing both Cr and Ni is needed.

In contrast to nickel, **iron** has a destabilizing effect on the  $\gamma/\gamma'$ -microstructure as shown in Figure 6 on two alloys containing 8 at.% and 16 at.% Fe. The alloy with 8 at.% Fe still exhibits a  $\gamma/\gamma'$ -microstructure. However, the volume fraction of the  $\gamma'$ -phase is lower than that of the ternary alloy indicating that Fe partitions to the  $\gamma$ -phase [2, 23]. Moreover, a formation of further intermetallic phases takes place, as shown in Figure 6a, which can be another reason for the decreased  $\gamma'$ -volume fraction if the  $\gamma'$ -forming element W is enriched in these needle-like intermetallic phases. The alloy with 16 at.% Fe does not consist of a  $\gamma/\gamma'$ -microstructure at all. Furthermore, increasing the Fe content substantially lowers the  $\gamma'$ -solvus temperature as shown in Table 1.

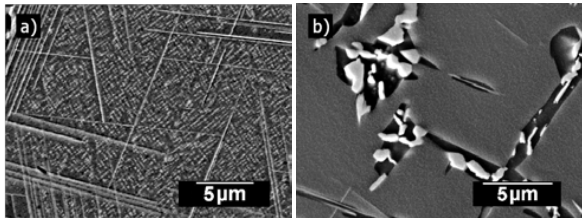


Figure 6: Microstructure of Fe containing alloys. a) 9W-8Fe-0.12B, b) 9W-16Fe-0.12B.

Similar to Ni-base superalloys [22], **titanium** partitions to the  $\gamma'$ -phase [23], which increases the solvus temperature and the volume fraction and therefore enhances the mechanical properties at high temperatures [14]. The  $\gamma/\gamma'$ -microstructure of the alloy 9W-2Ti-0.12B is shown in Figure 8a along with those of alloys containing Ta, Mo and Si which are discussed in the following. **Tantalum** partitions more strongly to  $\gamma'$ -phase than Ti [23], thus the volume fraction of the  $\gamma'$ -phase in the alloy 9W-2Ta-0.12B is slightly higher as seen in Figure 8b. Additionally, Ta substantially increases the  $\gamma'$ -solvus temperature (see Table 1 and [7, 9]).

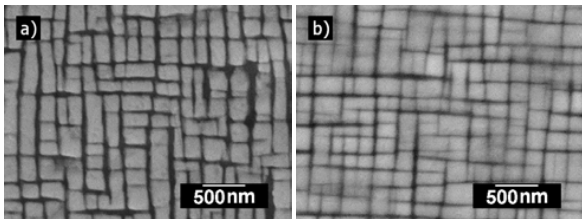


Figure 7: Microstructure of: a) 9W-2Ti-0.12B, b) 9W-2Ta-0.12B.

**Molybdenum** (Figure 8) and **vanadium** have a similar stabilizing effect on the  $\gamma'$ -phase, however, without a pronounced improvement of the mechanical properties [14]. The increase in the  $\gamma'$ -solvus temperature is moderate [14].

Addition of 2 at.% **silicon** enhances the oxidation resistance [10] and slightly increases the solvus temperature as well as the volume fraction of the  $\gamma'$ -phase (Table 1).

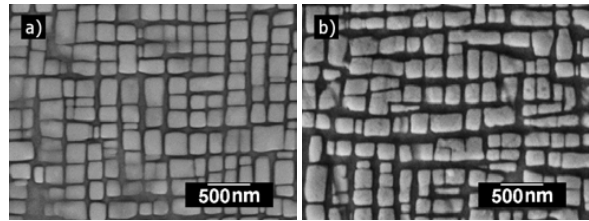


Figure 8: Microstructure of: a) 9W-1Mo-0.04B, b) 10W-2Si.

Addition of **iridium** has been studied in the Co-Al-W-Ta system [9]. It was shown to increase not only the  $\gamma'$ -solvus temperature, but also the liquidus temperature of the material [9] possibly due to the higher melting point and complete solid solubility in the Co-Ir system.

Addition of small amounts of **boron** (0.04-0.12at.%) leads to development of precipitates at the grain boundaries and prevents their decohesion during mechanical tests [9, 14], thus, a minimum amount of boron was added to all investigated alloys. However, the solubility of boron depends on the particular quaternary alloying element. In the case of Ta and Ti containing quaternary alloys the boron content has to be increased to enable the formation of the grain boundary precipitates (alloys 9W-2Ta-0.12B and 9W-2Ti-0.12B [14]) as shown in Figure 9. Noteworthy, addition of 2 at.% Si leads to analogous grain boundary precipitates. Further investigation are presented in chapter “Nanoindentation of grain boundaries”.

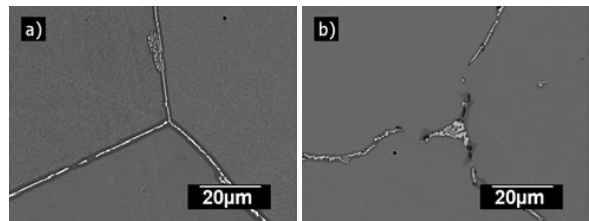


Figure 9: Morphology of the grain boundary precipitates in the alloys 9W-0.12B (a) and 9W-2Ti-0.12B (b).

#### Microstructure – long term phase stability

The experimental alloys investigated in this work were aged for 200 hrs at 900 °C. To investigate also the long term phase stability the samples were aged additionally for 1000 hrs at 900 °C. To assess the oversaturation of the alloys and stability against discontinuous precipitation and coarsening, additional aging with the same duration was performed on solution heat treated samples at 750 °C.

Long term aging at 900 °C shows for most alloys an increasing size of the  $\gamma'$ -precipitates (exceptions are alloys with Ir, Fe and high contents of Cr without Ni and will be discussed later in this section). No further phases have been formed showing that all alloy compositions should fall into the  $\gamma/\gamma'$ -two-phase region in the phase diagram. However, Tsukamoto et al. [24] reported that diffusion kinetics at the aging temperature might be too slow for phase transformations to take place in the given aging time, thus longer aging times have to be taken into consideration.

An exceptional behavior exhibits the alloy 9W-8Cr-0.04B which suffered from increased formation of intermetallic phases as well as W-rich phases as demonstrated in Figure 10. However, very small regions in-between still exhibit the  $\gamma/\gamma'$ -microstructure (Figure 10). Obviously, the oversaturation was decreased by the formation of further intermetallic phases leading to small two-phase regions with  $\gamma/\gamma'$ -microstructure.

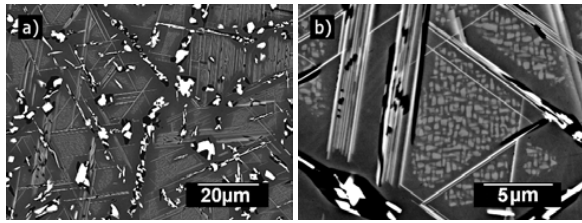


Figure 10: Microstructure evolution in the alloy 9W-8Cr-0.12B after aging for 1000 hrs at 900 °C.

Another exception is the alloy 8W-2Ta-2Ir. Discontinuous precipitation at grain boundaries takes place already after aging for 50 hrs as shown in Figure 11. After 400 hrs almost the whole  $\gamma/\gamma'$ -microstructure is transformed into lamellae of  $\text{Co}_3\text{W}$  and  $\text{CoAl}$  (Figure 12). Oversaturation of the matrix with the alloying elements is a possible explanation since the alloy variant with a reduced W concentration (5W-2Ta-2Ir) exhibits a stable microstructure after 400 hrs aging time [9].

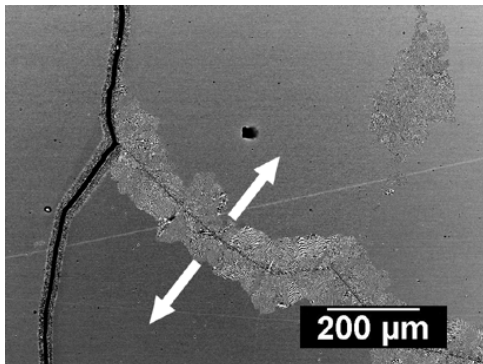


Figure 11: Discontinuous precipitation and coarsening starting from the grain boundaries in alloy 8W-2Ta-2Ir during aging at 900 °C for 50 hrs.

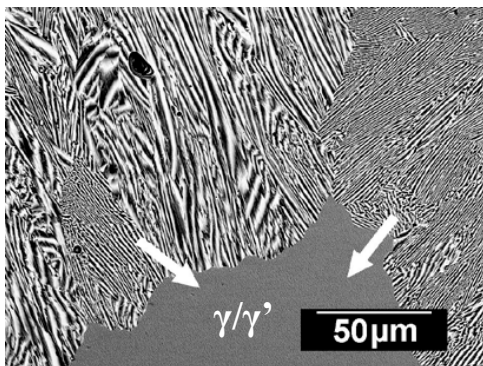


Figure 12: After aging for 400 hrs at 900 °C the  $\gamma/\gamma'$  - microstructure is almost discontinuously transformed.

Long term aging at 750 °C shows similar results as the experiments at 900 °C regarding the phase stability since no other phases have been formed in most alloys. However, the size of the  $\gamma'$ -precipitates present is much smaller (ca. 50-100 nm) due to decreased diffusion activity at the lower temperature. Noteworthy, the  $\gamma'$ -precipitates possess already a cuboidal shape. This is due to the high lattice misfit (see chapter "Misfit measurements") so that the reduction of coherency stresses by alignment along the [001]

directions is favored over the increase in surface energy, although the  $\gamma'$ -precipitate size is rather small.

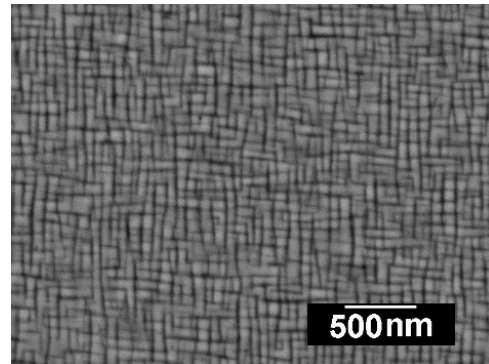


Figure 13: Microstructure of alloy 9W-0.08B aged for 1000 hrs at 750 °C. The size of the  $\gamma'$ -precipitates is less than 100 nm. The cuboidal  $\gamma'$ -shape is already present.

#### Nanoindentation of grain boundaries

As mentioned above, a sufficient high grain boundary strength is crucial for mechanical properties at high temperatures and can be achieved by the addition of small amounts of B (0.04-0.12 at.%). This leads to formation of a W-rich intermetallic phase along the grain boundaries accompanied with an adjacent  $\gamma'$ -free zone due to the depletion of tungsten, which is necessary for the formation of the  $\gamma'$ -phase. The overall volume fraction of such an arrangement is less than 1 volume percent. Nevertheless it is expected that the  $\gamma'$ -depleted zone influences the mechanical properties of the bulk material. Krol et al. have shown that similar  $\gamma'$ -precipitate free zones in polycrystalline Ni-base superalloys can lower the yield strength significantly if a certain width is exceeded [25]. An example is shown in Figure 14 [14]. The morphology of the grain boundaries is similar for the B-doped alloys and the Si-containing (B-free) alloy 10W-2Si.

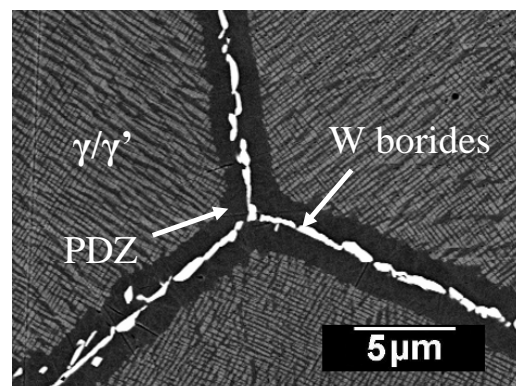


Figure 14: BSE micrograph of a typical grain boundary morphology with borides and an adjacent  $\gamma'$  precipitate depleted zone (PDZ) in the alloy 9W-0.12B.

The influence of the alloying elements on the precipitate depleted zone (PDZ) and its mechanical properties were investigated with nanoindentation. Figure 15 shows exemplarily an AFM image of the indented PDZ area.

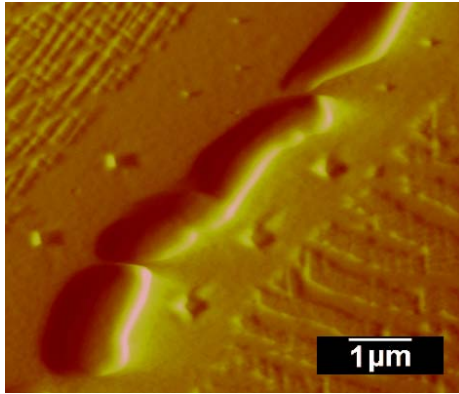


Figure 15: AFM image of a grain boundary with indentations in a boron-containing  $\gamma'$ -strengthened Co-base superalloy.

The load-displacement curves of the two investigated boron containing  $\gamma'$ -strengthened Co-base superalloys 9W-0.12B and 9W-2Ti-0.12B are shown in Figure 16.

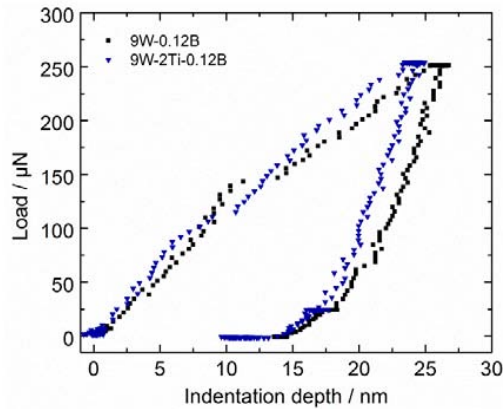


Figure 16: Load – displacement curves of the PDZs of alloys 9W-0.12B and 9W-2Ti-0.12B.

According to this data, the hardness of the PDZ in the Ti-containing alloy is more than 20% higher (9W-0.12B:  $5.1 \pm 0.2$  GPa; 9W-2Ti-0.12B:  $6.3 \pm 0.6$  GPa). This could be a result of solid solution strengthening due to the Ti addition. However, the formation energy of Ti borides is lower than that of W borides [26]. Thus, Ti contributes presumably to the formation of borides in the 9W-2Ti-0.12B alloy and a higher percentage of W will retain in the PDZ, compared to the 9W-0.12B alloy, and still act as solid solution hardener. As a result, in 9W-2Ti-0.12B alloy the PDZ hardness is higher.

#### Misfit measurements

In order to investigate whether the lattice misfit is positive at room temperature according to Sato et al. [2] and whether it remains positive at creep temperatures, high energy X-ray diffraction was performed to determine the lattice parameters of  $\gamma$  and  $\gamma'$  in the alloy 9W-0.12B. The (002) diffraction peaks recorded at room temperature and 850 °C are shown in Figure 17. At room temperature the (002) reflection is asymmetric. This means that the sub-peak coming from the  $\gamma$ -phase with its lower volume fraction is shifted towards higher  $2\theta$  values compared to the  $\gamma'$ -sub-peak. Accordingly, the alloy possesses a positive lattice

misfit at room temperature with lattice constants of 0.3581 nm for the  $\gamma$ -matrix and 0.3609 nm for the  $\gamma'$ -phase which are in good agreement with the values given by Sato et al [2]. This results in a positive lattice misfit of 0.8 % at room temperature. With increasing temperature the (002) peak becomes more symmetric and the amount of misfit decreases, but it is still positive with 0.4 % at 850 °C. The corresponding lattice constants of the  $\gamma$  and  $\gamma'$  phases are 0.3644 nm and 0.3657 nm, respectively. The reason for the decrease can be a combined effect of the different thermal expansion coefficients of the phases  $\gamma$  and  $\gamma'$ , the redistribution of alloying elements between  $\gamma$  and  $\gamma'$  and the change of the chemical composition mainly of the  $\gamma$ -phase due to a decreasing  $\gamma'$ -volume fraction with increasing temperature [27].

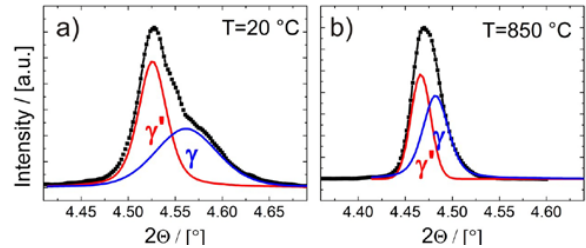


Figure 17: Recorded (002) diffractograms (dots) of alloy 9W-0.12B at a) room temperature and b) 850 °C. The fitted sub-peaks of both  $\gamma$  and  $\gamma'$  and the sum of the sub-peaks (line) are also shown.

#### Creep strength of $\gamma'$ hardened vs. conventional carbide hardened Co-base superalloys

The creep strength of the B-doped ternary alloy 9W-0.04B at 850 °C is by magnitudes superior to that of the wrought Co-base alloy Haynes 188 [14] and, as shown in Figure 18, also superior to the cast Co-base alloy Mar-M 509. Thus, the effect of the  $\gamma'$  hardening on creep strength is much stronger than that of carbide hardening and solid solution strengthening utilized in conventional Co-base superalloys.

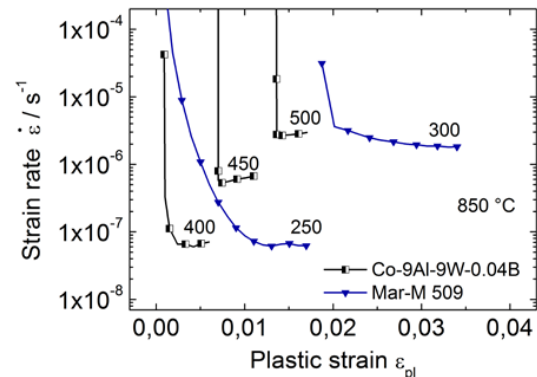


Figure 18: Creep curves of  $\gamma'$ -strengthened and conventional Co-base superalloys at 850 °C at various stress levels. Numbers next to the creep curves represent stress values in MPa. Experiments were performed with changes in stress levels in the secondary creep regime.



### Creep strength and microstructural evolution at different temperatures

Creep curves of the  $\gamma'$ -strengthened alloy 9W-0.12B at different temperatures are shown in Figure 19. The minimum of the strain rate was reached within the first percent of plastic deformation. This is preferable for turbine component applications due to restrictions in maximum tolerable strain in service.

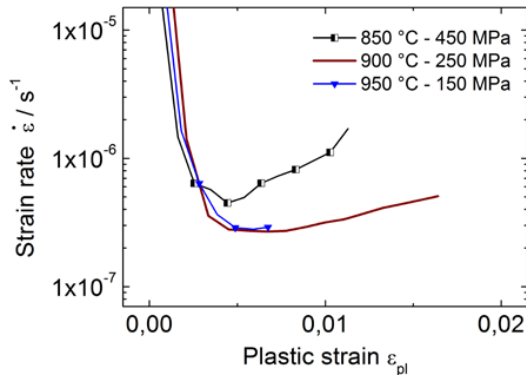


Figure 19: Creep curves of B-doped ternary alloys at different temperatures and applied constant stress.

From microstructural investigations on crept specimens it is evident that with increasing temperature the tendency to rafting increases. Figure 20 shows the microstructure after creep deformation parallel to the stress axis in the creep test.

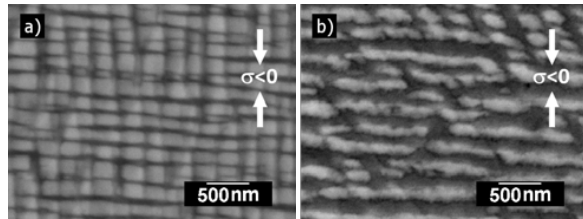


Figure 20: Microstructures of the alloy 9W-0.12B after creep at 850 °C and 450 MPa (a) and 950 °C and 150 MPa (b).

At 850 °C there is only a slight evidence of rafting visible, at 950 °C a fully rafted  $\gamma/\gamma'$ -microstructure has been developed which is oriented perpendicular to the stress axis confirming the positive misfit ( $a_{\gamma'} > a_{\gamma}$ ) in the alloy determined at 850 °C by means of high energy X-ray diffraction. However at 850 °C the diffusion kinetics are too slow for pronounced directional coarsening in the given creep time. In case of alloys with positive lattice misfit at creep temperature and compressive applied stress the deformation occurs preferably in the horizontal channels as shown schematically in Figure 21. Interfacial dislocations in the horizontal channels reduce the coherency induced tensile stresses in the  $\gamma$ -matrix parallel to the interface while they would add up to the coherency stresses in the vertical channels. Therefore dislocation movement in the horizontal  $\gamma$ -channels is preferred which is also shown in the TEM image of an [001] oriented grain (Figure 22) where matrix dislocations of  $a/2 \langle 101 \rangle \{111\}$  type in  $\gamma$  channels perpendicular to the external compressive stress axis are visible.

At 950 °C and low stresses rafting takes place to a high extent. The rafting process is caused by a superposition of external

applied stress on the coherency stresses due to the lattice misfit between the  $\gamma$ - and  $\gamma'$ -phase [28].

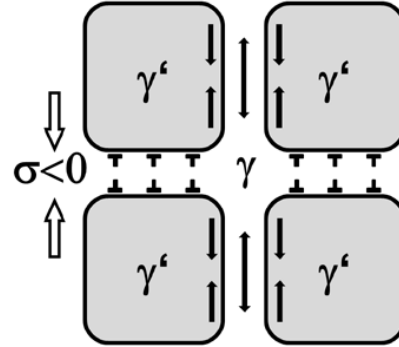


Figure 21: Schematic illustration of formation of interfacial dislocation networks at the onset of plastic deformation of an alloy with positive misfit under compression. Adopted from [28].

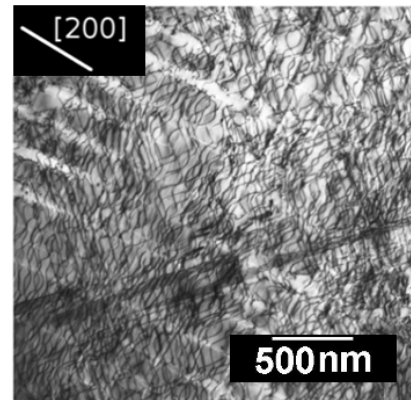


Figure 22: TEM image of a sample crept at 850 °C and 450 MPa showing matrix dislocations in matrix channels perpendicular to the stress axis in compression [14].

Through directional coarsening perpendicular to the compressive stress axis by exchange of  $\gamma$ - and  $\gamma'$ -forming elements from vertical to horizontal channels and vice versa the interfacial coherency stresses can be reduced [28, 29].

### Creep strength – Influence of alloying elements

The results of creep tests at 850 °C and 950 °C on the experimental alloys are shown in Figure 23 and Figure 24.

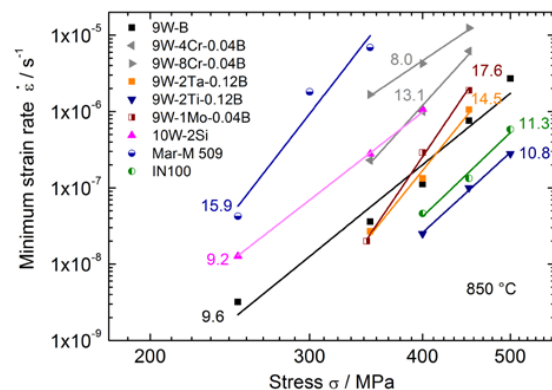


Figure 23: Norton plot of the alloys tested at 850 °C. Values next to the data lines represent corresponding stress exponents  $n$ .

The minimum strain rate is plotted as a function of applied constant stress. For better comparison, creep tests on conventional cast Co-base (Mar-M509) and cast Ni-base (IN100) superalloys were performed and added to the diagrams.

In general, at 850 °C the creep strength of the experimental alloys is between that of the conventional alloys Mar-M 509 and IN100 (some data have already been published in [14]). An exception is the 9W-2Ti-0.12B alloy exhibiting a creep strength higher than that of the Ni-base superalloy IN100.

The boron-doped ternary alloy 9W-B exhibits a comparable creep strength as its Ta- and Mo containing alloy variants. However, at lower stress levels the ternary alloy shows slightly lower creep strength and vice versa. Alloys 10W-2Si and 9W-4Cr-0.04B have a lower creep strength compared to alloy 9W-B but similar stress exponents. The alloy 9W-8Cr-0.04B exhibits the lowest creep strength of the investigated experimental alloys.

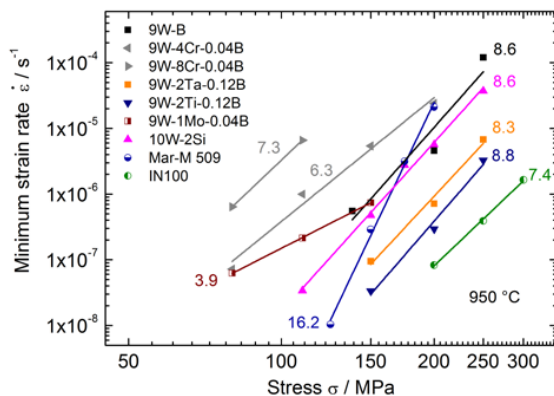


Figure 24: Norton plot of the alloys tested at 950 °C. Values next to the data lines represent corresponding stress exponents  $n$ .

Creep experiments at 950 °C showed that alloying of Ta and Ti has the highest impact on the creep strength.

In case of Ta the reason might be the more pronounced flow stress anomaly compared to the ternary alloy [7]. Additionally, Ta is known to be a low diffusing element in Ni [30]. Assuming that this is also true for Ta in Co, Ta increases the creep strength especially at higher temperatures as diffusion controlled processes play a more important role. Further reasons might be the substantially higher  $\gamma'$ -solvus temperature and the increased  $\gamma'$ -volume fraction of 82 %, compared to 58 % of alloy 9W-B (Table 1). However, both  $\gamma'$ -volume fractions differ from 70 % which is found to be the optimum for  $\gamma/\gamma'$ -Ni-base superalloys [31].

In contrast, the alloy 9W-2Ti-0.12B exhibits a  $\gamma'$ -volume fraction of 75 %, which might be one reason for the superior creep strength among the investigated Co-base alloys [14]. Further reasons might be the higher  $\gamma'$ -solvus temperature leading to a less pronounced reduction of  $\gamma'$ -volume fraction. Additionally Ti is known to be a  $\gamma'$ -strengthening element in Ni-base superalloys [20]. According to nanoindentation additions of Ti also increase the strength of the  $\gamma'$ -depleted zone which might hinder the dislocation movement in this area and thus contribute to the bulk creep strength.

However, at this temperature ( $T = 950$  °C) the creep strength of IN100 is superior to the 9W-2Ti-0.12B alloy possibly due to ca. 50 K higher  $\gamma'$ -solvus temperature of IN100 [32].

The 10W-2Si alloys performed comparable to the ternary alloy. Cr-containing alloys exhibit again the lowest creep strength of all investigated experimental alloys. The degradation of the  $\gamma/\gamma'$ -microstructure in addition to formation of further W-rich intermetallic phases could be one possible explanation. Additionally, at 950 °C the low  $\gamma'$  solvus temperature might lead to dissolution of the  $\gamma'$  precipitates and are another reason for the low creep strength.

At both test temperatures the stress exponents were calculated from the collected data and are presented on the diagrams. Even though there is a slight variation at each temperature, the overall values of the stress exponents decrease with increasing temperature. The only exception is the conventional Co-base alloy Mar-M 509 exhibiting almost the same stress exponent at 850 °C and 950 °C. This alloy has only a small volume fraction of the strengthening phase (carbides), though the creep behavior is governed by the pure matrix, which is more sensitive to stress variations than alloys possessing high volume fraction of a precipitation phase [33]. Furthermore, the creep strength of Mar-M 509 at 950 °C is comparable to the 9W-0.12B and 10W-2Si alloys. A possible reason might be partial dissolution of the  $\gamma'$ -phase in both Co-base alloys at that temperature due to a relatively low  $\gamma'$  solvus temperature (Table 1), while the carbides in Mar-M 509 are still stable. Indeed, the  $\gamma'$ -solvus temperatures of 9W-2Ta-0.12B and 9W-2Ti-0.12B, which exhibit better creep strength, are more than 130 K above the creep temperature of 950 °C.

## Conclusions

- (1) Ti and Ta effectively enhance the creep strength of Co-base superalloys at 950 °C. Ti containing alloys exhibit creep strength comparable with Ni-base superalloy IN100 at 850 °C.
- (2)  $\gamma'$ -hardened Co-base superalloys are superior to conventional solid solution and carbide strengthened Co-base alloy MarM 509 in terms of creep strength at 850 °C and 950 °C.
- (3) Formation of W-rich borides along the grain boundaries are necessary for grain boundary strengthening during creep but also leads to an adjacent  $\gamma'$ -depleted zone. Ti increases the hardness of the precipitate depleted zone.
- (4) The lattice misfit of the ternary alloy Co-9Al-9W with boron additions has been proven to be positive from room temperature up to 950 °C based on the orientation of the rafted microstructure and high resolution X-ray diffraction measurements.
- (5) High contents of Cr and Fe destabilize the  $\gamma/\gamma'$ -microstructure. However, addition of Ni widen the  $\gamma/\gamma'$ -two phase field, since no additional intermetallic phases are present in alloys containing Cr plus Ni. Discontinuous precipitation is observed only in the Ir-containing alloy during aging. In all other alloys no formation of further intermetallic phases are found even after 1000 hrs aging at 750 °C and 900 °C.

## Acknowledgements

Authors are grateful for the financial support of the German Science Foundation (DFG) within the framework of DFG graduate school 1229. Authors would also like to acknowledge



Kurt Beyer for the arc melting of various alloys, Peter Randelzhofer for the DSC measurements, Natalie Kömpel for the GDOES measurements and Svitlana Rosen for nanoindentation measurements.

# References

- [1] C. T. Sims, N. S. Stoloff and W. C. Hagel. *Superalloys II*. John Wiley & Sons, New York, United States of America, 1987.
- [2] J. Sato, T. Omori, K. Oikawa, I. Ohnuma, R. Kainuma and K. Ishida. *Science*, 312:90–91, 2006.
- [3] P. Viatour, J.M. Drapier and D. Coursouradis. *Cobalt*, 3:67–74, 1973.
- [4] K. Shinagawa, T. Omori, J. Sato, K. Oikawa, I. Ohnuma, R. Kainuma and K. Ishida. *Materials Transactions*, 49(6):1474–1479, 2008.
- [5] S. Kobayashi, Y. Tsukamoto, T. Takasugi, H. Chinen, T. Omori, K. Ishida, and S. Zaefferer. *Intermetallics*, 17(12):1085 – 1089, 2009.
- [6] S. Kobayashi, Y. Tsukamoto and T. Takasugi. *Intermetallics*, 19(12):1908 – 1912, 2011.
- [7] A. Suzuki and T. M. Pollock. *Acta Materialia*, 56(6):1288 – 1297, 2008.
- [8] K. Shinagawa, T. Omori, K. Oikawa, R. Kainuma and K. Ishida. *Scripta Materialia*, 61(6):612 – 615, 2009.
- [9] A. Bauer, S. Neumeier, F. Pyczak and M. Göken. *Scripta Materialia*, 63(12):1197 – 1200, 2010.
- [10] L. Klein, A. Bauer, S. Neumeier, M. Göken and S. Virtanen. *Corrosion Science*, 53(5):2027 – 2034, 2011.
- [11] L. Klein, Y. Shen, M.S. Killian and S. Virtanen. *Corrosion Science*, 53(9):2713 – 2720, 2011.
- [12] C. Jiang. *Scripta Materialia*, 59(10):1075 – 1078, 2008.
- [13] M. Chen and C. Wang. *Scripta Materialia*, 60(8):659 – 662, 2009.
- [14] A. Bauer, S. Neumeier, F. Pyczak, R. F. Singer and M. Göken. *Materials Science and Engineering A*, Accepted, 2012.
- [15] F. Pyczak, B. Devrient and H. Mughrabi. Proc. 10<sup>th</sup> Int. Symposium on Superalloys, Superalloys 2004, eds. K. A. Green et al. (Warrendale, PA: The Minerals, Metals and Materials Society, 2004), pp. 827–836.
- [16] A. Heckl, S. Neumeier, M. Göken and R.F. Singer. *Materials Science and Engineering: A*, 528(9):3435 – 3444, 2011.
- [17] S. Neumeier, F. Pyczak and M. Göken. Proc. 11<sup>th</sup> Int. Symposium on Superalloys, Superalloys 2008, eds. R. C. Reed et al. (Warrendale, PA: The Minerals, Metals and Materials Society, 2008), pp. 109–119.
- [18] W.C. Oliver and G.M. Pharr. *Journal of Materials Research*, 7(6):1564–1580, 1992.
- [19] W.C. Oliver and G.M. Pharr. *Journal of Materials Research*, 19(1):3–20, 2004.
- [20] R. C. Reed. *The Superalloys*. Cambridge University Press, Cambridge, United Kingdom, 2006.
- [21] D. Coutsouradis, A. Davin and M. Lamberigts. *Materials Science and Engineering*, 88:11–19, 1987.
- [22] C.C. Jia, K. Ishida and T. Nishizawa. *Metallurgical and Materials Transactions A*, 25(3):473–485, 1994.
- [23] K. Ishida. *Mater. Res. Soc. Symp. Proc.*, Vol. 1128, 357–368, 2009.
- [24] Y. Tsukamoto, S. Kobayashi and T. Takasugi. *Materials Science Forum*, 654-656:448–451, June 2010.
- [25] T. Krol, D. Baither and E. Nembach. *Acta Materialia*, 52(7):2095 – 2108, 2004.
- [26] A. N. Kolmogorov and S. Curtarolo. *Physical Review B - Condensed Matter and Materials Physics*, 74(22), 2006.
- [27] Yu.N. Gornostyrev, O.Yu. Kontsevoi, K.Yu. Khromov, M.I. Katsnelson, and A.J. Freeman. *Scripta Materialia*, 56(2):81 – 84, 2007.
- [28] H. Mughrabi and U. Tetzlaff. *Advanced Engineering Materials*, 2(6):319–326, 2000.
- [29] T.M. Pollock and A.S. Argon. *Acta Metallurgica et Materialia*, 42(6):1859 – 1874, 1994.
- [30] C.L. Fu, R. Reed, A. Janotti and M. Krcmar. Proc. 10<sup>th</sup> Int. Symposium on Superalloys, Superalloys 2004, eds. K. A. Green et al. (Warrendale, PA: The Minerals, Metals and Materials Society, 2004), pp. 867–876.
- [31] T. Murakumo, T. Kobayashi, Y. Koizumi and H. Harada. *Acta Materialia*, 52(12):3737 – 3744, 2004.
- [32] J.P. Dennison, P.D. Holmes and B. Wilshire. *Materials Science and Engineering*, 33(1):35 – 47, 1978.
- [33] B. Reppich, M. Heilmaier, K. Liebig, G. Schumann, K. Stein and T. Woller. *Steel Research*, 61(6):251–257, 1990.